ARTICLE

Spin Crossover in Iron(II) Hofmann Clathrates Analogues with 1,2,3-triazole

Received 00th January 20xx,
Accepted 00th January 20xx

DOI: 10.1039/x0xx00000x

Iryna S. Kuzevanova,[a,b] Olesia I. Kucheriv,[a,c] Volodymyr M. Hiiuk,[a,c] Dina D. Naumova,[a] Sergiu Shova,*[d] Sergii I. Shylin,[e] Volodymyr O. Kotsyubynsky,[f] Aurelian Rotaru,[g] Igor O. Fritsky[a,c] and Il'ya A. Gural'skiy* [a,c]

Hofmann-like cyanometallic complexes represent one of the biggest and well-known classes of Fe^{II} spin-crossover compounds. In this paper, we report on the first Fe^{II} Hofmann clathrate analogues with unsubstituted 1,2,3-triazole, which exhibit temperature induced spin transition. Two new coordination polymers with the general formula $[Fe^{II}(1,2,3\text{-triazole})_2M^{II}(CN)_4]$ (M =Pt, Pd) undergo abrupt hysteretic spin crossover in the range of 190–225 K as revealed by magnetic susceptibility measurements. Two compounds are isostructural and are built of infinite cyanometallic layers which are supported by 1,2,3-triazole ligands. The thermal hysteresis loop is very stable at different scan rates from 0.5 to 10 K min^{-1}. The compounds display strong thermochromic effect, changing their colour from pink in the low-spin state to white in the high-spin state. Our findings show that 1,2,3-triazole is suitable for elaboration of spin-crossover Hofmann clathrate analogues, and its use instead of more classical azines can advantageously expand this family of complexes.

Introduction

Spin-crossover (SCO) complexes represent a huge class of switchable materials that can change between low-spin (LS) and high-spin (HS) states under the influence of various external stimuli. Spin transition can be triggered by the change of temperature[1] or pressure,[2] light irradiation,[3] magnetic field,[4] or inclusion of various guest molecules. The transition is accompanied by a drastic change of magnetic,[5] optical,[6] mechanical,[7] and electric properties[8]. As well, the cooperativity of SCO frequently leads to a hysteretic character of the transition. Such bistability, in turn, results in effect of molecular memory of the material, i.e., the ability to exist in different states under the same external conditions. These important features of SCO materials open numerous opportunities for their application as thermochromic materials,[9] chemical sensors,[10] MEMS,[7] microthermometers,[11] microwave switches,[12,13] etc.

Among all classes of SCO materials, Hofmann-like coordination polymers[14] attract considerable attention due to the universal approach towards their synthesis, huge variety of suitable ligands, ability to drastically change SCO characteristics upon guest effect, etc. Hofmann-like clathrates are 2D and 3D coordination polymers that are assembled of cyanobimetallic layers supported by N-donor heterocyclic ligands. While the original Hofmann framework $[Ni(NH_3)_2Ni(CN)_4]\cdot 2C_6H_6$ was obtained in 1897,[15] the first analogue exhibiting SCO behavior $[Fe(py)_2Ni(CN)_4]$ was obtained by Kitazawa *et al.* only in 1996.[16] This finding provoked a wave of discoveries of new compounds of this type which now constitute one of the biggest classes of SCO complexes.

Various strategies have been proposed for modification of SCO Hofmann-type coordination compounds, such as introduction of different N-donor ligands; use of square-planar, linear or dodecahedral cyanometallic linkers; inclusion of guest molecules,[17,18] etc.

Ligands with simple architectures, such as unsubstituted pyridine,[19] diazines[19–23] and their substituted analogues[24,25] have been shown to be appropriate building blocks for construction of SCO active cyanometallic complexes.[26] As well, bicyclic ligands, such as naphthyridines,[27,28] phthalazine[29] and quinoline[20,30–32] have been in a focus of the most recent studies. Meanwhile, there are much fewer examples of Hofmann clathrate analogues where axial co-ligands of Fe^{II} are represented by azoles.[33–38] Moreover, those are represented by 1,2,4-triazoles with bulky substituents such as 4-(2-pyridyl)-1,2,4-triazole,[33] N-thiophenylidene-4H-1,2,4-triazol-4-amine,[38] (E)-1-phenyl-N-(1,2,4-triazol-4-yl)methanimine,[36] etc.[39]

Here we describe two new SCO Hofmann clathrates analogues based on unsubstituted 1,2,3-triazole: $[Fe(1,2,3\text{-triazole})_2M(CN)_4]$ where M = Pt (**Pt-trz**) and Pd (**Pd-trz**).

[a] *Department of Chemistry, Taras Shevchenko National University of Kyiv, Volodymyrska St. 64, Kyiv 01601, Ukraine. E-mail: illia.guralskyi@univ.kyiv.ua;*
[b] *Department of General and Inorganic Chemistry, National Technical University of Ukraine "Igor Sikorsky Kyiv Polytechnic Institute", Peremogy Pr. 37, Kyiv 03056, Ukraine;*
[c] *UkrOrgSyntez Ltd., Chervonotkatska St. 67, Kyiv 02094, Ukraine.*
[d] *Department of Inorganic Polymers, Petru Poni Institute of Macromolecular Chemistry, Aleea Grigore Ghica Voda 41-A, Iasi 700487, Romania;*
[e] *Department of Chemistry – Ångström Laboratory, Uppsala University, 75120 Uppsala, Sweden;*
[f] *Department of Material Science and New Technology, Vasyl Stefanyk Precarpathian National University, Ivano-Frankivsk 76018, Ukraine;*
[g] *Faculty of Electrical Engineering and Computer Science &MANSiD Research Center, Stefan cel Mare University, Universitatii St. 13, Suceava 720229, Romania.*

† Electronic Supplementary Information (ESI) available: IR, crystal data and refinement details. See DOI: 10.1039/x0xx00000x

Results and discussion

Crystal Structure

Crystal structures of **Pt-trz** were obtained at 255 K and 170 K. This complex crystalizes in the *Imma* space group with four formula units $Fe(1,2,3\text{-trz})_2M(CN)_4$ per cell (Table 1). A fragment of its structure illustrating a coordination environment of iron(II) is demonstrated in Figure 1a. Iron(II) ion is situated on an inversion centre; it has $[FeN_6]$ coordination environment of slightly elongated octahedron. Specifically, the iron(II) centre is equatorially coordinated by four N atoms that belong to four equivalent centrosymmetric square-planar tetracyanoplatinate anions [Fe1–N1 = 2.136(5) Å (255 K) and Fe1–N1 = 1.936(6) Å (170 K)], while axial positions are occupied by two 1-coordinated 1,2,3-triazole molecules [Fe1–N2 = 2.199(8) Å (255 K) and Fe1–N2 = 1.974(9) Å (170 K)] (Table 2). The difference in the Fe–N bond length at different temperatures is caused by the temperature induced SCO, that is further confirmed by magnetic measurements. The length distortion parameter for the HS structure (255 K) $\zeta = \Sigma_{i=1}^{6}|(Fe–N_i)\text{-}<Fe–N>| = 0.165$ Å is larger than for the LS $\zeta = 0.100$ Å structure indicating greater deviation from ideal octahedron for the complex in the HS state. The distances between iron(II) centre and N atoms of 1,2,3-triazole are longer than those between Fe^{II} and tatracyanoplatinate. This effect is related to a lower affinity of iron(II) cation to the neutral organic ligand comparing to the negatively charged $[Pt(CN)_4]^{2-}$ anion. The deviation from the ideal octahedron of twelve *cis*-N–Fe–N angels can be described by the octahedral distortion parameter $\Sigma = \Sigma_{i=1}^{12}|90° - \alpha_i| = 5.74°$ (255 K) and $\Sigma = 1.86°$ (170 K). Trigonal distortion parameter $\Theta = \Sigma_{i=1}^{24}|60° - \beta_i| = 17.0°$ (255 K) and $\Theta = 10.2°$ (170 K), where β are 24 unique torsion angles between the adjacent N atoms on opposite triangular faces viewed along the pseudo-threefold axes. These parameters indicate there is a weak distortion of octahedron in the LS state. It is important to note, that distortion parameters should always be very carefully used to judge on the spin state of Fe^{II} centres, as it depends on many different factors such as symmetry of the structure (e.g. involved atoms on special positions), measurement temperature, etc.

The crystal packing is shown in Figure 1b. The coordination framework is connected by bridging tetracyanoplatinate moieties into an infinite two-dimensional grid. The 2D $[FePt(CN)_4]$ layers are corrugated due to deviation from linearity of Fe1–N1–C1 and N1–C1–Pt1 angles (Table 2). Additionally, the crystal structure is characterized by the presence of N–H···N hydrogen bonding between the neighbouring 1,2,3-triazole molecules. Moreover, the H atom involved in hydrogen bonding is disordered between two positions and can be bonded to N3 or N4 atom with equal probability (Figure S1). Bond lengths and angles between atoms involved in hydrogen bonding are given in Table 2. Additionally, the structure is stabilized by π–π contacts (Figure 1c) with centroid–centroid distances 3.7299(8) Å (255 K) and 3.6413(15) Å (170 K). Such set of weak interactions contributes to the creation of a supramolecular 3D framework.

Single crystals of **Pd-trz** could not be obtained of quality sufficient for single crystal X-ray diffraction measurements, and conclusion about its structure is based on the PXRD analysis (Figure 2). PXRD patterns of **Pt-trz** and **Pd-trz** display similar set of peaks confirming that these complexes are isostructural.

Table 1. Crystallographic parameters of **Pt-trz**.

Temperature/K	170	255
Empirical formula	$C_8H_6FeN_{10}Pt$	$C_8H_6N_{10}FePt$
Formula weight	493.17	493.17
Crystal system	orthorhombic	orthorhombic
Space group	*Imma*	*Imma*
a/Å	13.8736(9)	14.3717(6)
b/Å	7.1949(4)	7.4268(3)
c/Å	12.8934(15)	13.1817(13)
α/°	90	90
β/°	90	90
γ/°	90	90
Volume/Å^3	1287.01(19)	1406.96(16)
Z	4	4
ρ_{calc}g/cm^3	2.545	2.328
μ/mm^{-1}	11.991	10.969
F(000)	912.0	912.0
Goodness-of-fit on F^2	1.114	1.062
Final R indexes [I>=2σ (I)]	$R_1 = 0.0415$, $wR_2 = 0.0882$	$R_1 = 0.0351$, $wR_2 = 0.0742$
Final R Indexes [all data]	$R_1 = 0.0512$, $wR_2 = 0.0937$	$R_1 = 0.0449$, $wR_2 = 0.0789$

$R_1 = \Sigma||F_o|-|F_c||/\Sigma|F_o|$ and $wR_2 = [\Sigma w(F_o^2 - F_c^2)_2/\Sigma w(F_o^2)^2]^{1/2}$ for $F_o^2 > 2\sigma(F_o^2)$.

Among the already published Fe^{II} Hofmann clathrate analogues the most similar to **Pt-trz** are complexes with unsubstituted monodentate azines: pyridine,[40] pyridazine[21] and pyrimidine,[41] which have general composition $[Fe(L)_2M(CN)_4]\cdot nH_2O$.

The general structure and ligation manner in these complexes are similar, however, they crystalize in *Cmmm* space group on contrast to **Pt-trz**,. The main structural differences originate from corrugation of cyanometallic layers in **Pt-trz**, which are flat in complexes with azines. In both cases cyanometallic layers create 4,4-nets which are constructed by quadrangles. In complexes with azines π–π interactions between aromatic ligands are directed along the smaller diagonals, however in **Pt-trz** triazole rings are oriented to create π–π contacts along the longer diagonals of quadrangles in cyanometallic layers. Consequently, in order to favour π–π interactions cyanometallic layers get corrugated thus bringing the triazole rings closer.

Magnetic Properties

Following the magnetic susceptibility as a function of temperature allows to monitor spin transition because the change in the number of unpaired electrons leads to a distinct change of susceptibility. The plots of $\chi_M T$ vs. T (where χ_M is the molar magnetic susceptibility and T is the temperature) **for Pt-trz** and **Pd-trz** recorded in 100 – 300 K temperature range at 2 K min^{-1} scan rate are shown in Figure 3.

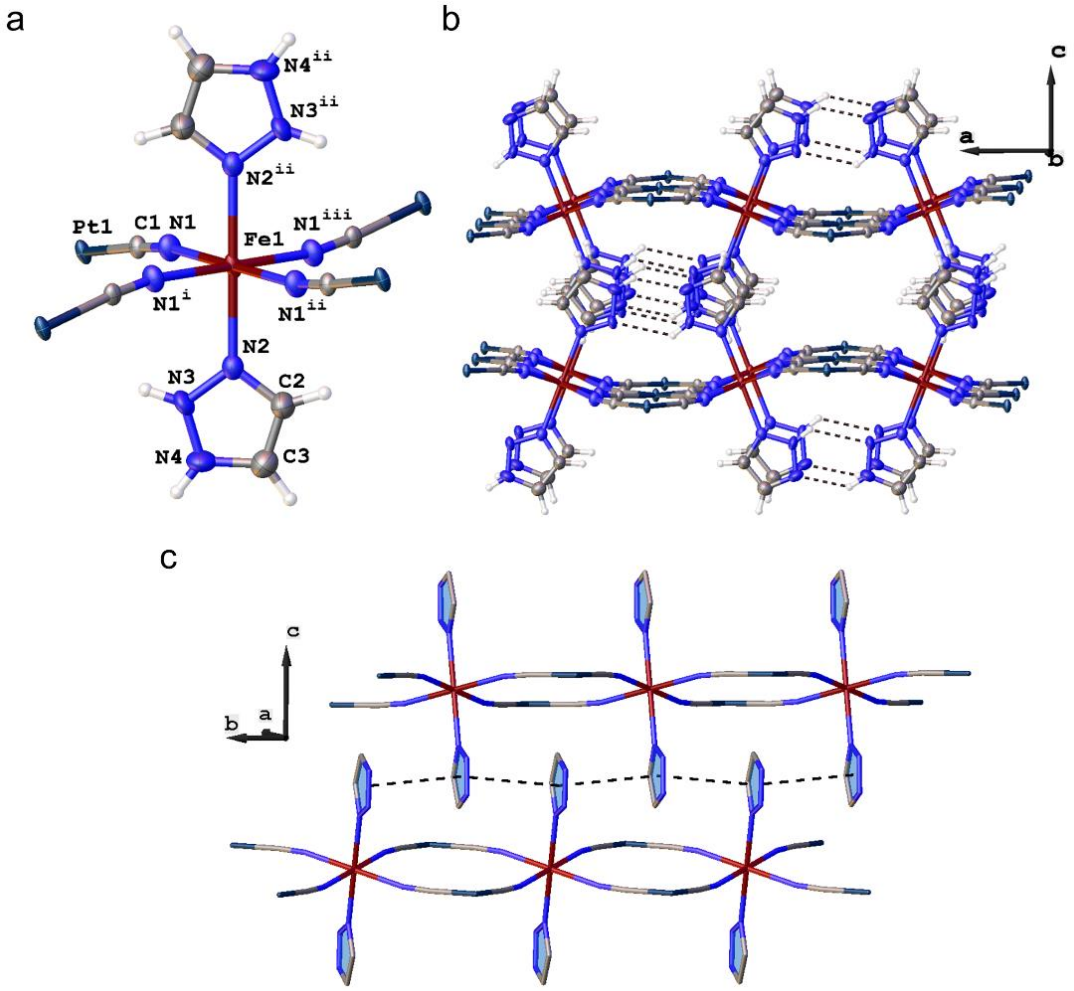

Figure 1. (a) Fragment of the crystal structure of **Pt-trz** showing atom labelling scheme. Displacement ellipsoids are shown with 50% probability. H atoms at N3 and N4 have 0.5 chemical occupancies due to the disorder. Symmetry codes: (i) +x, 3/2-y, +z; (ii) 3/2-x, 3/2-y, ½-z; (iii) 3/2-x, +y, 1/2-z. (b) View of the crystal structure of **Pt-trz** in the *ac* plane demonstrating infinite 2D layers. (c) Fragment of the crystal structure showing π–π contacts as dashed lines.

Table 2. Selected bond distances [Å] and angles [°] of **Pt-trz** in HS and LS forms.

	HS (255 K)	LS (170 K)
Fe1–N1 [Å]	2.136(5)	1.936(6)
Fe1–N2 [Å]	2.199(8)	1.974(9)
<Fe–N> [Å]	2.157	1.949
V_{oct} [FeN_6] [Å^3]	13.380	9.861
Σ [°]	5.74	1.86
Θ [°]	17.0	10.2
ζ [Å]	0.165	0.100
π–π [Å]	3.7299(8)	3.6413(15)
N3···N3^a [Å]	3.084(15)	3.097(18)
N4···N4^a [Å]	2.872(19)	2.869(19)
Fe1–N1–C1[°]	170.0(6)	174.6(6)
Pt1–C1–N1 [°]	176.0(6)	174.0(7)
C1–Pt1–C1 [°]	177.0	175.9
N3–H···N3 [°]	128.3	127.3
N4–H···N4 [°]	136.5	137.9

$\zeta = \Sigma_{i=1}^{6}|(Fe–N_i)-<Fe–N>|$, $\Sigma = \Sigma_{i=1}^{12}|90° - \alpha_i|$, $\Theta = \Sigma_{i=1}^{24}|60° - \beta_i|$

For **Pt-trz** (Figure 3a) the $\chi_M T$ value at 300 K equals 3.74 cm^3 K mol^{-1} indicating that all Fe^{II} centres are in the HS state. This value stays constant down to 204 K. Upon further cooling the transition to the LS state occurs in poorly distinguishable twounequal steps reaching $\chi_M T$ of 0.65 cm3 K mol^{-1} at 187 K. According to the first derivative, $T_{\downarrow 1}$ = 194 K with small plateau at 197 K. The second step is observed at $T_{\downarrow 2}$ = 200 K. In the heating mode transition back to the HS state occurs at $T_{\uparrow 1}$ = 210 K and $T_{\uparrow 2}$ = 222 K with a small plateau around 214 K. The difference in the temperature of spin transition leads to occurrence of hysteresis loops with ΔT1 = 16 K and ΔT2 = 12 K. The transition in **Pd-trz** is similar to that observed in **Pt-trz**. At 300 K the $\chi_M T$ value of **Pd-trz** is 3.65 cm^3 K mol^{-1} and stays unchanged down to temperature of 208 K where the start of the spin transition is observed. In case of **Pd-trz** the SCO in cooling mode occurs in one step at $T_{\downarrow}$ = 202 K. The $\chi_M T$ value decreases down to 0.81 cm^3 K mol^{-1} at 191 K. At further heating the LS → HS transition occurs in two unequal steps at $T_{\uparrow 1}$ = 212 K. The small plateau is observed at 214 K. The second step takes place at $T_{\uparrow 2}$ = 220 K. The resulting hysteresis loop is ΔT_1 = 10 K and ΔT_2 = 18 K.

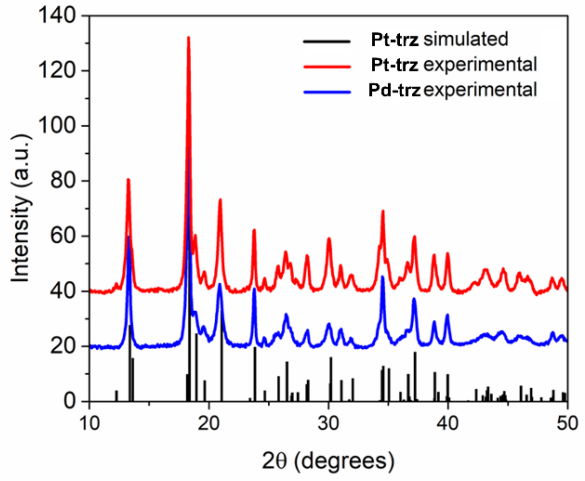

Figure 2. Experimental PXRD patterns of Pt-trz and Pd-trz, and pattern of Pt-trz simulated from single crystal structure (255 K). Good correspondence between patterns confirms that complexes Pt-trz and Pd-trz are isostructural.

The step character of SCO can probably originate from the structural disorder of H(N) atoms in triazolic rings that provide slightly different coordination environments of Fe^{II} ions (Figure S2). Due to the disorder of H atoms all Fe^{II} centres are crystallographically identical and therefore cannot be assigned to different steps of SCO. A similar effect has already been observed for $[Fe(Mepz)_2\{Au(CN)_2\}_2]$ SCO Hofmann clathrate analogue.[42] However there a more bulky methyl group is statistically disordered which leads to more pronounced steps. Additionally, the influence of H atom in the *ortho*-position to the donor nitrogen can be observed in a series of $[Fe(L)_2M(CN)_4]$ where M = Pt, Pd and L = pyridine,[19] pyridazine,[21] pyrimidine[20] complexes. These three pairs of complexes are isostructural and have very similar ligands, however the transition temperatures in pyridine and pyrimidine analogues are ca. 40 – 65 K lower than in pyridazine based complexes. Despite evident electronic factors, the absence of one hydrogen atom in the *ortho*-position of a ligand facilitates the contraction of the Fe – N bonds upon transition to the LS state that results in increase of transition temperature. Transition temperatures of 2D Hofmann clathrates analogues with unsubstituted azines and some selected azoles are summarized in Table S1.

^{57}Fe Mössbauer Spectroscopy

SCO can additionally be monitored by the change of isomer shift and quadrupole splitting in ^{57}Fe Mossbauer spectra, as these parameters differ significantly for the LS and the HS forms of Fe^{II}. At room temperature Mössbauer spectra of both **Pt-trz** and **Pd-trz** are characterized by the presence of one doublet (Figure 4), the hyperfine parameters of which indicate that both complexes are in the HS state (**Pt-trz**: δ^{HS} = 1.052(1) mm s^{-1}, ΔEq^{HS} = 1.509(2) mm s^{-1}; **Pd-trz**: δ^{HS} = 1.080(1) mm s^{-1}, ΔEq^{HS} = 1.495(3) mm s^{-1}; Table 3). At 214 K, which corresponds to the temperature of plateau in **Pt-trz** and **Pd-trz** in the heating mode, the relative intensity of the HS doublets decreases to 73% and 74%, respectively. At this temperature the LS doublets emerge indicating the presence of 27% and 26% of LS fractions in **Pt-trz** and **Pd-trz** complexes, respectively, that

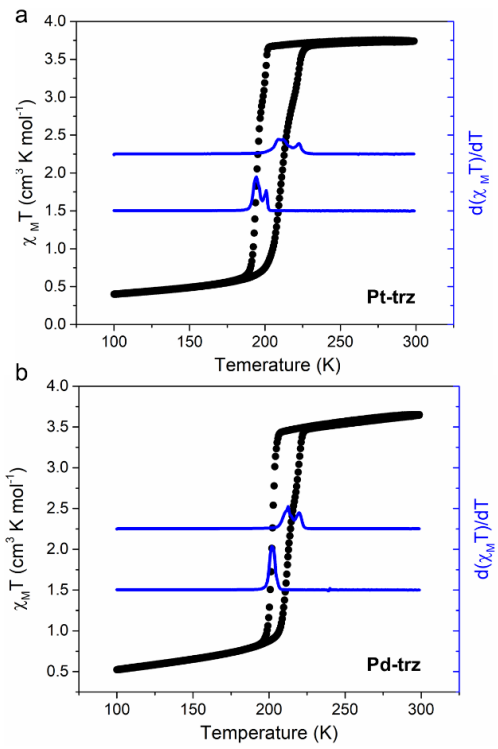

Figure 3. $\chi_M T$ vs. T plots (black dots) for **Pt-trz** (a) and **Pd-trz** (b) in heating and cooling modes showing abrupt temperature induced spin transitions in these complexes. The first derivative of $\chi_M T$ vs. T plots is shown as a blue line.

well correlates with magnetic measurements (**Pt-trz**: δ^{HS} = 1.213(1) mm s^{-1}, ΔEq^{HS} = 2.025(3) mm s^{-1}, δ^{LS} = 0.403(2) mm s^{-1}, ΔEq^{LS} = 0.348(3) mm s^{-1}; **Pd-trz**: δ^{HS} = 1.187(1) mm s^{-1}, ΔEq^{HS} = 2.051(3) mm s^{-1}, δ^{LS} = 0.393(2) mm s^{-1}, ΔEq^{LS} = 0.350(5) mm s^{-1}). At 80 K the relative intensities of the LS doublets increase reaching 92% for **Pt-trz** and 90% for **Pd-trz**. Simultaneously, HS doublets do not disappear completely, these doublets intensities decrease indicating the presence of 8% and 10% of residual HS fractions in **Pt-trz** and **Pd-trz**, respectively (**Pt-trz**: δ^{HS} = 1.254(2) mm s^{-1}, ΔEq^{HS} = 2.410(11) mm s^{-1}, δ^{LS} = 0.438(1) mm s^{-1}, ΔEq^{LS} = 0.381(2) mm s^{-1}; **Pd-trz**: δ^{HS} = 1.218(2) mm s^{-1}, ΔEq^{HS} = 2.453(10) mm s^{-1}, δ^{LS} = 0.423(1) mm s^{-1}, ΔEq^{LS} = 0.392(2) mm s^{-1}). In addition, in both complexes quadrupole splitting of the HS doublet is ca. 0.90-0.96 mm s^{-1} larger at 80K then at 293 K. This effect originates from increased difference in population of d_{xy} and d_{xz}/d_{yz} levels at low temperature which contributes to temperature-dependent electric field gradient, this effect is frequently observed for HS Fe^{II} compounds.[43] Simultaneously, in the LS form d_{xy}, d_{xz} and d_{yz} orbitals are fully occupied and consequently ΔEq^{LS} does not depend much on temperature.

Calorimetric Measurements

SCO is characterized by an entropy change originated from the variation of both spin multiplicity and vibrational frequencies. These thermodynamic effects can be followed via calorimetric measurements (usually in DSC technique). **Pt-trz** shows two endothermic peaks in heating mode with $T_{\uparrow 1}$ = 212 K, $T_{\uparrow 2}$ = 222 K (Figure 5). Upon cooling, on contrast to magnetic measurements, two steps of transition are not resolved, resulting in one exothermic peak with $T_{\downarrow}$ = 189 K.

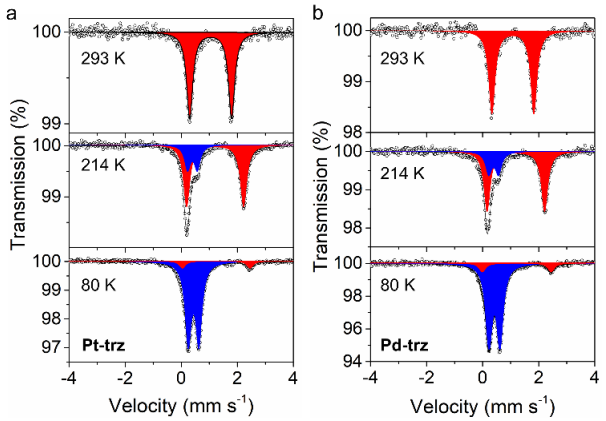

Figure 4. ^{57}Fe Mössbauer spectra of **Pt-trz** and **Pd-trz**, recorded at 80, 214 and 293 K showing HS and LS doublets in red and blue, respectively.

Table 3. Hyperfine parameters for **Pt-trz** and **Pd-trz** deived from their Mössbauer spectra.

Compound	T (K)	Spin state	δ (mm s^{-1})	ΔEq (mm s^{-1})	Content (%)
Pt-trz	293	HS	1.052(1)	1.509(2)	100
	214	HS	1.213(1)	2.025(3)	73(2)
		LS	0.403(2)	0.348(3)	27(2)
	80	HS	1.254(2)	2.410(11)	8(3)
		LS	0.438(1)	0.381(2)	92(2)
Pd-trz	293	HS	1.080(1)	1.495(3)	100
	214	HS	1.187(1)	2.051(3)	74(2)
		LS	0.393(2)	0.350(5)	26(3)
	80	HS	1.218(2)	2.453(10)	10(2)
		LS	0.423(1)	0.392(2)	90(2)

In the complex **Pd-trz** transition to the LS state occurs at $T_{\downarrow}$ = 198 K, upon heating two endothermic peaks are observed at $T_{\uparrow 1}$ = 215 K and $T_{\uparrow 2}$ = 222 K. Transition temperatures, obtained from DSC measurements are in the similar temperature interval with those, obtained in magnetic experiments. Among other factors, a different thermalization in two experiments should contribute to the observed difference of transition temperatures. Thermodynamic parameters of spin transition in **Pt-trz** and **Pd-trz** are summarized in Table 4. Enthalpy and entropy change values are in range of $|\Delta H|$ = 8 – 10 kJ mol^{-1} and $|\Delta S|$ = 44 – 49 J K^{-1} mol^{-1}, which are typical for Fe^{II} SCO Hofmann clathrate analogues.[14]

Optical Measurements

Spin transition is accompanied by a drastic thermochromic effect which is associated with changes of *d-d* transition band. Thus, the colour change allows to monitor temperature induced spin transition in complexes by detecting intensity of the reflected light and analysis of microphotographs (Figure S3). Optical reflectance of complexes **Pt-trz** and **Pd-trz** as a function of temperature is shown in Figure 6. The values of transition temperatures, obtained in optical experiments are consistent with those, obtained in magnetic measurements: for **Pt-trz** $T_{\downarrow}$ = 185 K and $T_{\uparrow}$ = 212 K and for **Pd-trz** $T_{\downarrow}$ = 193 K and $T_{\uparrow}$ = 218 K. At the same time, stepped character of transition is not observed as the plateau is too small to be detected in optical experiments. Transition temperatures of **Pt-trz** and **Pd-trz** obtained in different experiments are summarized in Table S2.

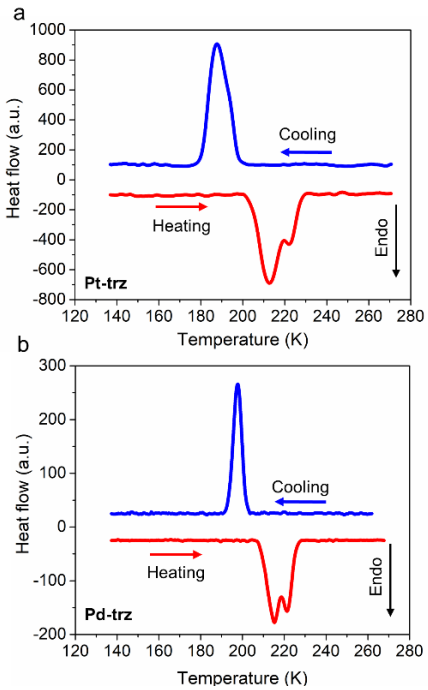

Figure 5. DSC curves of **Pt-trz** (a) and **Pd-trz** (b) showing thermal anomalies upon SCO. Measurements were performed at 10 K min^{-1} scan rate.

The scan rate dependent measurements are an important part of the analysis of SCO systems. Since the shape, sharpness and/or position of the hysteresis loop may be scan rate dependent.[44] In previous studies, one can find many remarkable examples when the SCO behaviour directly depends on this factor.[45–47]

Therefore, we performed scan rate dependent measurements for single crystals of **Pt-trz**. Temperature dependence of the normalized reflectance recorded upon cooling and heating (in the range 193-236 K) at scan rates of 0.5–10 K min^{-1} is given in Figure 7.

The scan rate study displayed stable hysteretic SCO behaviour with abrupt transitions in both cooling and heating modes. The thermal hysteresis loops (~28 K wide) are obtained with high reproducibility. The transition temperatures ($T_{\downarrow}$ = 198.7(6) K and $T_{\uparrow}$ = 226.7(13) K) are not scan rate dependent and are constant within the scan rate range 0.5 – 10 K min^{-1} (Table S3). Similar SCO behaviour has already been observed in recent research, for example, the

Table 4. Data obtained from DSC measurements of **Pt-trz** and **Pd-trz**.

	Pt-trz	**Pd-trz**
$T_{\downarrow}$ (K)	189	198
$T_{\uparrow}$ (K)	1st 212	1st 215
	2nd 222	2nd 222
$\Delta H_{\downarrow}$ (kJ mol^{-1})	-8.4	-9.3
$\Delta H_{\uparrow}$ (kJ mol^{-1})	10.5	9.9
$<\|\Delta H\|>$ (kJ mol^{-1})	9.5	9.6
$\Delta S_{\downarrow}$ (J K^{-1} mol^{-1})	-44.4	-47.0
$\Delta S_{\uparrow}$ (J K^{-1} mol^{-1})	48.4	45.3
$<\|\Delta S\|>$ (J K^{-1} mol^{-1})	46.4	46.2

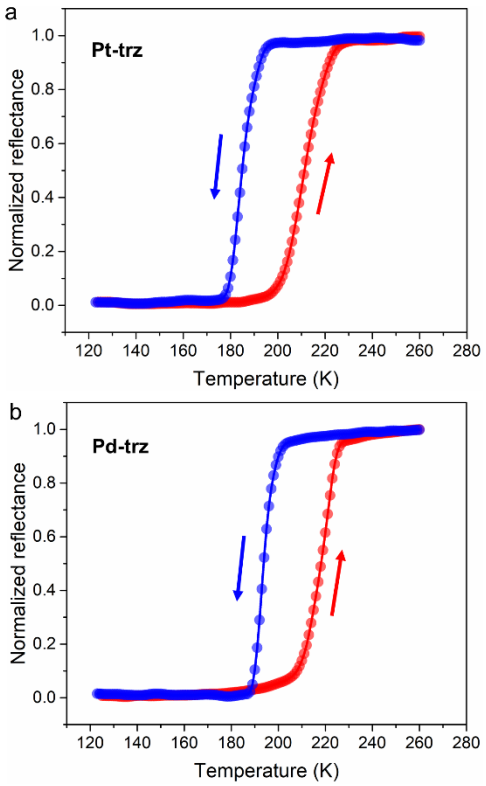

Figure 6. Normalized reflectance of **Pt-trz** (a) and **Pd-trz** (b) as a function of temperature measured at 10 K min^{-1} scan rate.

absence of kinetic phenomena was detected for single crystals of the SCO complex of composition [Fe(HB(tz)$_3$)$_2$] (where tz = 1,2,4-triazol-1-yl).[48,49] There is a certain temperature shift observed between measurements with single crystals and bulk powders. This effect is frequently observed for SCO complexes and originates from different degree of crystallinity, specific defect or other factors.[28]

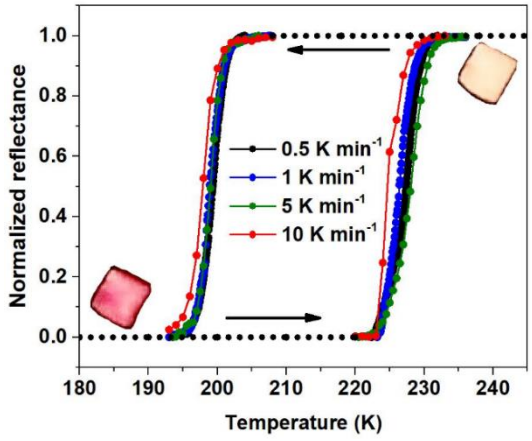

Figure 7. Scan rate study (0.5−10 K min−1) of normalized reflectance vs. temperature for single crystals of **Pt-trz**.

Conclusions

In summary, using of 1,2,3-triazole as the axial ligand allowed to obtain two new spin-crossover 2D Hofmann clathrates analogues with general formula [Fe(1,2,3-trz)$_2$M(CN)$_4$] (M = Pt, Pd). These complexes have similar structural features as 2D Fe^{II} Hofmann clathrate analogues with azines that allowed direct comparison of their properties. Both of the obtained complexes display abrupt hysteretic temperature induced spin transitions which occur in two non-equivalent steps. The stepped character is most likely associated with the disorder of H-atoms in triazole ring.

Drastic thermochromic effect which accompanies spin transition in these complexes allowed to perform scan rate dependent optical measurements for single crystals of a Pt based complex. It is shown that the key SCO characteristics of this complex are constant and do not depend on the rate of heating or cooling.

This study demonstrates that 1,2,3-triazoles constitute another class of ligands, suitable for formation of spin crossover active Hofmann clathrates analogues. Additionally, future modification of this ligand with different small substitutes can allow to obtain new complexes with different temperatures, abruptness and completeness of spin transitions.

Experimental information

Materials

1,2,3-triazole was obtained from UkrOrgSynthez Ltd., potassium tetracyanoplatinate and potassium tetracyanopalladate were obtained from Abcr and used as received. Iron(II) toluenesulphonate was obtained as previously described by Coucouvanis.[50]

Synthesis

Powder samples

Powders of **Pt-trz** and **Pd-trz** were obtained by adding 1 mmol (5 eq.) of 1,2,3-triazole solution in 0.6 ml of water to the solution of 0.2 mmol (1 eq.) of $K_2[Pt(CN)_4]$ (for **Pt-trz**) or $K_2[Pd(CN)_4]$ (for **Pd-trz**) in 0.5 ml of water. Afterwards, a solution of 0.2 mmol (1 eq.) $Fe(OTs)_2{\cdot}6H_2O$ in 0.5 ml of water was added to the mixture. White precipitate appeared immediately, was separated by centrifugation, washed with water and dried on air. Yields were 84 % for **Pt-trz** and 82% for **Pd-trz**. Elemental analysis for $C_8H_6FeN_{10}Pt$ (**Pt-trz**): calc. C, 19.47; H, 1.22; N, 28.40; found C, 19.42; H, 1.25; N, 28.31. $C_8H_6FeN_{10}Pd$ (**Pd-trz**): calc. C, 23.76; H, 1.49; N, 34.65; found C, 23.69; H, 1.42; N, 34.67. FTIR spectra of **Pt-trz** and **Pd-trz** are shown in Figures S4-S5.

Single crystals

Single crystals of **Pt-trz** were obtained by a slow-diffusion method within three layers in a 3.5 ml tube: the first layer was a solution of 0.05 mmol of $K_2[Pt(CN)_4]$ and 0.025 mmol of 1,2,3-triazole in 1 ml of water; the second layer was 1.5 ml of water:methanol (1:2) mixture; the third layer was a solution of $Fe(OTs)_2{\cdot}6H_2O$ 0.05 mmol in 0.5 ml of methanol. After three weeks transparent crystals appeared in the middle layer; they

were collected and kept in the mother solution prior to measurements.

Physical measurements

X-ray diffraction. Single crystal X-ray diffraction measurements for **Pt-trz** were performed using Oxford-Diffraction XCALIBUR E CCD diffractometer with graphite-monochromated Mo-Kα radiation. Data were collected at 170 and 255 K. The data integration and determination of the unit cell were performed using CrysAlisPro package from Oxford Diffraction. The structures were solved with ShelXT using intrinsic phasing methods and refined with ShelXL using least-squares minimization.[51,52] Olex2 was used as graphical interface for ShelX programmes.[53] Non-hydrogen atoms were refined as anisotropic. All hydrogen atoms were placed geometrically and refined as riding. Distortion parameters were calculated using OctaDist software.[54] Crystallographic data for the structures have been deposited with the Cambridge Crystallographic Data Centre, CCDC: 2083162, 2083163. Crystallographic information for **Pt-trz** is summarized in Tables S4-S5.

Magnetic measurements. Magnetic susceptibilities of **Pt-trz** and **Pd-trz** as a function of temperature were measured in the temperature range of 100-300 K using a MPMS3 SQUID magnetometer (Quantum Design Inc.), in DC mode, under a DC magnetic field of 1000 Oe. Cooling and heating rates were 2 K/min. All data were corrected for the diamagnetic contributions of the sample holder and the samples estimated from Pascal's constants.

Differential scanning calorimetry. DSC measurements were performed using Linkam DSC 600 stage operating at scan rate of 10 K min $^{-1}$.

Optical reflectance measurements. Optical microscopy images of the same crystal have been recorded in reflection mode during heating/cooling cycles at different temperature scan rates ranging from 0.5 to 10 K min^{-1}. The system for monitoring the SCO by changing the intensity of the reflected light consisted of an optical microscope MICROmed XS-8530 equipped with the CCD camera MICROmed 5.0 mPix for measurements of single crystals and optical microscope Optica SZM-1 equipped with the camera Sigeta UCMOS 1300 for powder samples. The sample temperature was controlled with a Linkam optical cryostat DSC600. Image processing was performed using ImageJ software.

PXRD measurements. The PXRD patterns were acquired on Shimadzu XRD-6000 diffractometer using Cu-Kα radiation (5-50 ° range, 0.05° step).

Elemental analyses and FTIR. Elemental analyses (CHN) were performed with a Vario Micro Cube (Elementar) CHNOS elemental analyzer. FTIR spectra were recorded with Perkin-Elmer spectrometer BX II (4000–400 cm^{-1}) in Nujol.

^{57}Fe-Mössbauer spectra were recorded using a constant acceleration Mössbauer spectrometer equipped with a liquid nitrogen cryostat. A ^{57}Co source embedded in a Rh matrix with an active diameter of 4.5 mm and activity of ~25 mCi was used. The emitted γ-rays penetrated the sample and 14.4 keV γ-rays were detected in transmission geometry. Fitting of the experimental data was performed with Recoil software.[55] Hyperfine parameters uncertainties were evaluated from the covariance matrix of the fit. Isomer shifts are given relatively to iron metal at room temperature.

Conflicts of interest

There are no conflicts to declare.

Acknowledgements

We acknowledge financial support from the Ministry of Education and Science of Ukraine (grants No. 19BF037-01M, 19BF037-04) and European program "Horizon 2020" within the framework of RISE (Research and innovation Staff exchange) scheme (grant No. 734322, Multifunctional Spincrossover Materials, SPINSWITCH). Dr. M. Seredyuk is acknowledged for some useful comments on the structural part.

Keywords: Spin crossover, Hofmann clathrate analogues, iron(II), 1,2,3-triazole, crystal structure, molecular bistability

Notes and references

1 P. Gütlich and H. A. Goodwin, *Spin Crossover Transit. Met. Compd. I*, 2012, **1**, 1–47.

2 A. B. Gaspar, V. Ksenofontov, M. Seredyuk and P. Gütlich, *Coord. Chem. Rev.*, 2005, **249**, 2661–2676.

3 P. Gütlich, A. Hauser and H. Spiering, *Angew. Chem. Int. Ed.*, 1994, **33**, 2024–2054.

4 Y. Qi, E. W. Müller, H. Spiering and P. Gütlich, *Chem. Phys. Lett.*, 1983, **101**, 503–505.

5 L. Cambi and L. Szegö, *Berichte der Dtsch. Chem. Gesellschaft (A B Ser.)*, 1931, **64**, 2591–2598.

6 A. Hauser, in *Spin Crossover in Transition Metal Compounds I*, eds. P. Gütlich and H. A. Goodwin, Springer-Verlag: Berlin/Heidelberg, 2004, pp. 49–58.

7 H. J. Shepherd, I. A. Gural'skiy, C. M. Quintero, S. Tricard, L. Salmon, G. Molnár and A. Bousseksou, *Nat. Commun.*, 2013, **4**, 2607.

8 A. Rotaru, I. A. Gural'skiy, G. Molnár, L. Salmon, P. Demont and A. Bousseksou, *Chem. Commun.*, 2012, **48**, 4163.

9 L. G. Lavrenova and O. G. Shakirova, *Eur. J. Inorg. Chem.*, 2013, **2013**, 670–682.

10 M. Ohba, K. Yoneda, G. Agustí, M. Carmen Muñoz, A. B. Gaspar, J. A. Real, M. Yamasaki, H. Ando, Y. Nakao, S. Sakaki and S. Kitagawa, *Angew. Chem. Int. Ed.*, 2009, **48**, 4767–4771.

11 L. Salmon, G. Molnár, D. Zitouni, C. Quintero, C. Bergaud, J.-C. Micheau and A. Bousseksou, *J. Mater. Chem.*, 2010, **20**, 5499–5503.

12 O. I. Kucheriv, V. V Oliynyk, V. V Zagorodnii, V. L. Launets, O. V. Penkivska, I. O. Fritsky and I. A. Gural'skiy, *RSC Adv.*, 2020, **10**, 21621–21628.

13 O. I. Kucheriv, V. V. Oliynyk, V. V. Zagorodnii, V. L. Launets and I. A. Gural'skiy, *Sci. Rep.*, 2016, **6**, 38334.

14 M. Carmen Muñoz and J. A. Real, *Coord. Chem. Rev.*, 2011, **255**, 2068–2093.

15 K. A. Hofmann and F. Küspert, *Zeitschrift für Anorg. Chemie*, 1897, **15**, 204–207.

16 T. Kitazawa, Y. Gomi, M. Takahashi, M. Takeda, M. Enomoto, A. Miyazaki and T. Enoki, *J. Mater. Chem.*, 1996, **6**, 119.

17 Z.-P. Ni, J.-L. Liu, M. N. Hoque, W. Liu, J.-Y. Li, Y.-C. Chen and M.-L. Tong, *Coord. Chem. Rev.*, 2017, **335**, 28–43.

18 R. Ohtani and S. Hayami, *Chem. Eur. J.*, 2017, **23**, 2236–2248.

19 V. Niel, J. M. Martinez-Agudo, M. Carmen Muñoz, A. B. Gaspar and J. A. Real, *Inorg. Chem.*, 2001, **40**, 3838–3839.

20 C. Bartual-Murgui, V. Rubio-Giménez, M. Meneses-Sánchez, F. J. Valverde-Muñoz, S. Tatay, C. Martí-Gastaldo, M. C. Muñoz and J. A. Real, *ACS Appl. Mater. Interfaces*, 2020, **12**, 29461–29472.

21 I. A. Gural'skiy, S. I. Shylin, V. Ksenofontov and W. Tremel, *Eur. J. Inorg. Chem.*, 2019, **2019**, 4532–4537.

22 V. Niel, A. Galet, A. B. Gaspar, M. Carmen Muñoz and J. A. Real, *Chem. Commun.*, 2003, **3**, 1248–1249.

23 V. Niel, A. L. Thompson, M. Carmen Muñoz, A. Galet, A. E. Goeta and J. A. Real, *Angew. Chem. Int. Ed.*, 2003, **42**, 3760–3763.

24 W. Liu, L. Wang, Y.-J. Su, Y.-C. Chen, J. Tucek, R. Zboril, Z.-P. Ni and M.-L. Tong, *Inorg. Chem.*, 2015, **54**, 8711–8716.

25 O. I. Kucheriv, S. I. Shylin, V. Ksenofontov, S. Dechert, M. Haukka, I. O. Fritsky and I. A. Gural'skiy, *Inorg. Chem.*, 2016, **55**, 4906–4914.

26 O. I. Kucheriv, I. O. Fritsky and I. A. Gural'skiy, *Inorganica Chim. Acta*, 2021, **521**, 120303.

27 L. Piñeiro-López, F. J. Valverde-Muñoz, M. Seredyuk, C. Bartual-Murgui, M. Carmen Muñoz and J. A. Real, *Eur. J. Inorg. Chem.*, 2018, **2018**, 289–296.

28 V. M. Hiiuk, S. Shova, A. Rotaru, V. Ksenofontov, I. O. Fritsky and I. A. Gural'skiy, *Chem. Commun.*, 2019, **55**, 3359–3362.

29 V. M. Hiiuk, S. Shova, A. Rotaru, A. A. Golub, I. O. Fritsky and I. A. Gural'skiy, *Dalton Trans.*, 2020, **49**, 5302–5311.

30 Y. C. Chen, Y. Meng, Y. J. Dong, X. W. Song, G. Z. Huang, C. L. Zhang, Z. P. Ni, J. Navařík, O. Malina, R. Zbořil and M. L. Tong, *Chem. Sci.*, 2020, **11**, 3281–3289.

31 Y. Meng, Q.-Q. Sheng, M. N. Hoque, Y.-C. Chen, S.-G. Wu, J. Tucek, R. Zboril, T. Liu, Z.-P. Ni and M.-L. Tong, *Chem. Eur. J.*, 2017, **23**, 10034–10037.

32 F. Setifi, E. Milin, C. Charles, F. Thétiot, S. Triki and C. J. Gómez-García, *Inorg. Chem.*, 2014, **53**, 97–104.

33 E. Milin, V. Patinec, S. Triki, E.-E. Bendeif, S. Pillet, M. Marchivie, G. Chastanet and K. Boukheddaden, *Inorg. Chem.*, 2016, **55**, 11652–11661.

34 N. F. Sciortino, F. Ragon, K. A. Zenere, P. D. Southon, G. J. Halder, K. W. Chapman, L. Piñeiro-López, J. A. Real, C. J. Kepert and S. M. Neville, *Inorg. Chem.*, 2016, **55**, 10490–10498.

35 N. F. Sciortino, K. A. Zenere, M. E. Corrigan, G. J. Halder, G. Chastanet, J. F. Létard, C. J. Kepert and S. M. Neville, *Chem. Sci.*, 2016, **8**, 701–707.

36 M. J. Murphy, K. A. Zenere, F. Ragon, P. D. Southon, C. J. Kepert and S. M. Neville, *J. Am. Chem. Soc.*, 2017, **139**, 1330–1335.

37 K. A. Zenere, S. G. Duyker, E. Trzop, E. Collet, B. Chan, P. W. Doheny, C. J. Kepert and S. M. Neville, *Chem. Sci.*, 2018, **9**, 5623–5629.

38 Y. M. Klein, N. F. Sciortino, F. Ragon, C. E. Housecroft, C. J. Kepert and S. M. Neville, *Chem. Commun.*, 2014, **50**, 3838–3840.

39 A. T. Brennan, K. A. Zenere, C. J. Kepert, J. K. Clegg and S. M. Neville, *Inorg. Chem.*, 2021, **60**, 3871–3878.

40 S. Sakaida, K. Otsubo, O. Sakata, C. Song, A. Fujiwara, M. Takata and H. Kitagawa, *Nat. Chem.*, 2016, **8**, 377–383.

41 V. Rubio-Giménez, G. Escorcia-Ariza, C. Bartual-Murgui, C. Sternemann, M. Galbiati, J. Castells-Gil, J. A. Real, S. Tatay and C. Martí-Gastaldo, *Chem. Mater.*, 2019, **31**, 7277–7287.

42 S. I. Shylin, O. I. Kucheriv, S. Shova, V. Ksenofontov, W. Tremel and I. A. Gural'skiy, *Inorg. Chem.*, 2020, **59**, 6541–6549.

43 P. B. Merrithew, P. G. Rasmussen and D. H. Vincent, *Inorg. Chem.*, 1971, **10**, 1401–1406.

44 S. Brooker, *Chem. Soc. Rev.*, 2015, **44**, 2880–2892.

45 R. Kulmaczewski, J. Olguín, J. A. Kitchen, H. L. C. Feltham, G. N. L. Jameson, J. L. Tallon and S. Brooker, *J. Am. Chem. Soc.*, 2014, **136**, 878–881.

46 M. Seredyuk, M. C. Muñoz, M. Castro, T. Romero-Morcillo, A. B. Gaspar and J. A. Real, *Chem. Eur. J.*, 2013, **19**, 6591–6596.

47 R. G. Miller, S. Narayanaswamy, J. L. Tallon and S. Brooker, *New J. Chem.*, 2014, 38, 1932–1941.

48 K. Ridier, S. Rat, L. Salmon, W. Nicolazzi, G. Molnár and A. Bousseksou, *Phys. Chem. Chem. Phys.*, 2018, **20**, 9139–9145.

49 K. Ridier, S. Rat, H. J. Shepherd, L. Salmon, W. Nicolazzi, G. Molnár and A. Bousseksou, *Phys. Rev. B*, 2017, **96**, 134106.

50 D. Coucouvanis, *Inorganic Syntheses*, John Wiley & Sons, Inc., USA, 2002, vol. 33.

51 G. M. Sheldrick, *Acta Crystallogr. Sect. C Struct. Chem.*, 2015, **71**, 3–8.

52 G. M. Sheldrick, *Acta Crystallogr. Sect. A Found. Adv.*, 2015, **71**, 3–8.

53 O. V. Dolomanov, L. J. Bourhis, R. J. Gildea, J. A. K. Howard and H. Puschmann, *J. Appl. Crystallogr.*, 2009, **42**, 339–341.

54 R. Ketkaew, Y. Tantirungrotechai, P. Harding, G. Chastanet, P. Guionneau, M. Marchivie and D. J. Harding, *Dalton Trans.*, 2021, **50**, 1086–1096.

55 K. Lagarec and D. G. Rancourt, *Nucl. Instruments Methods Phys. Res. Sect. B Beam Interact. with Mater. Atoms*, 1997, **129**, 266–280.